nature materials

Article

https://doi.org/10.1038/s41563-024-01972-3

A nuclear jamming transition in vertebrate organogenesis

Received: 2 August 2022

Accepted: 11 July 2024

Published online: 12 August 2024

Check for updates

Sangwoo Kim[1,5,6], Rana Amini[2,6], Shuo-Ting Yen[2], Petr Pospíšil[2], Arthur Boutillon[2], Ilker Ali Deniz[2] & Otger Campàs[1,2,3,4]

Jamming of cell collectives and associated rigidity transitions have been shown to play a key role in tissue dynamics, structure and morphogenesis. Cellular jamming is controlled by cellular density and the mechanics of cell–cell contacts. However, the contribution of subcellular organelles to the physical state of the emergent tissue is unclear. Here we report a nuclear jamming transition in zebrafish retina and brain tissues, where physical interactions between highly packed nuclei restrict cellular movements and control tissue mechanics and architecture. Computational modelling suggests that the nuclear volume fraction and anisotropy of cells control the emerging tissue physical state. Analysis of tissue architecture, mechanics and nuclear movements during eye development show that retina tissues undergo a nuclear jamming transition as they form, with increasing nuclear packing leading to more ordered cellular arrangements, reminiscent of the crystalline cellular packings in the functional adult eye. Our results reveal an important role of the cell nucleus in tissue mechanics and architecture.

Many developmental processes, including tissue morphogenesis and homoeostasis, require a tight control of the tissue architecture and its physical state[1,2]. Ordered cellular packings play important functional roles in several organs, such as the inner ear[3] or the eye[4,5], whereas disordered cellular states are important for cell mixing at different developmental stages[6]. Similarly, the emergent mechanical state of tissues (for example, fluid/solid states) and its spatiotemporal control have been shown to play an important role in tissue morphogenesis[6–12], cell dynamics[13–15], cell differentiation[11,16] and even tumour growth[17–19]. Connecting the emergent physical states of the tissue at supracellular scales to the underlying processes that control them at cellular and subcellular scales is essential for understanding how cells orchestrate embryonic development[20].

The physical state of embryonic tissues emerges from the collective physical interactions among cells. Mirroring inert systems, such as colloidal glasses, foams and emulsions[21], glassy dynamics and characteristics of cellular jamming, as well as other rigidity transitions, have been reported in cell monolayers in vitro[18,22,23]. More recently, rigidity transitions (jamming/glass transitions, fluid–solid transitions or tissue fluidization) have been observed in vivo within developing embryos and shown to play important functional roles[6,8,11,12,16]. Previous theoretical works have described the dynamics of cell collectives using various methodologies and predicted several observed behaviours, including different rigidity transitions[7,24–29]. To describe physical interactions among cells, these studies accounted for the structures that are generally thought to mediate mechanical interactions between cells, namely, cortical tension, cell adhesion and traction forces, but neglected any organelles. Although most organelles do not directly contribute to the mechanical interactions between cells, large ones could potentially play an important role in the emergent physical state of cell collectives, specifically embryonic tissues.

The cell nucleus is the largest organelle in cells and is considerably stiffer than other cellular structures[30]. In tissues with cells much larger than their nuclei, the emergent mechanical state of the tissue is dominated by cell surface mechanics[1,2,20]. However, during embryonic development, cells in different tissues and organs feature varying cell

[1]Department of Mechanical Engineering, University of California, Santa Barbara, CA, USA. [2]Cluster of Excellence Physics of Life, TU Dresden, Dresden, Germany. [3]Max Planck Institute of Molecular Cell Biology and Genetics, Dresden, Germany. [4]Center for Systems Biology Dresden, Dresden, Germany. [5]Present address: Institute of Mechanical Engineering, École Polytechnique Fédérale de Lausanne (EPFL), Lausanne, Switzerland. [6]These authors contributed equally: Sangwoo Kim, Rana Amini. e-mail: otger.campas@tu-dresden.de

https://doi.org/10.1038/s41563-024-01972-3

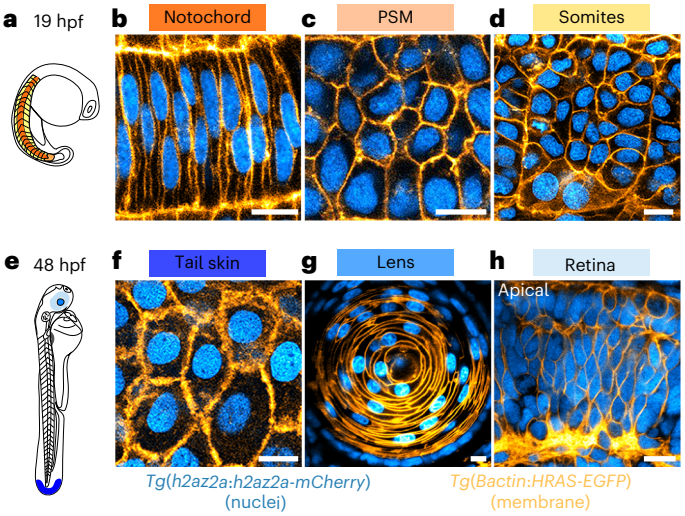

Fig. 1 | Varying nuclear volume fraction and anisotropy in various zebrafish tissues. a,**e**, Schematic of a zebrafish embryo at 19 hpf (**a**) and 48 hpf (**e**). **b**–**d**,**f**–**h**, Representative confocal sections through different tissues of transgenic embryos with membrane (*Tg*(*Bactin*:*HRAS-EGFP*); orange) and nuclear (*Tg*(*h2az2a*:*h2az2a-mCherry*); cyan) markers at 19 hpf (notochord (**b**); presomitic mesoderm (PSM) (**c**); somites (**d**)) and 48 hpf (tail skin (**f**); lens (**g**); retina (**h**)). Scale bars, 10 µm.

and nuclear sizes, with some cells being very large compared with their nuclei and others having nuclei nearly as large as the whole cell. Variations in the ratio between nucleus and cell volume (or nuclear–cytoplasmic ratio), namely, the nuclear volume fraction, occur throughout embryonic development, and abnormal changes have been associated with malignant transformations in some tissues[31,32]. These observations indicate that nuclear mechanical interactions may not be negligible in many tissues, as previously suggested for syncytial embryos[33–35] or in conditions leading to local nuclear crowding[36,37]. More generally, it is unclear how collective cell dynamics and the emergent tissue physical state and architecture may be affected by mechanical interactions among nuclei.

Here we study—both theoretically and experimentally—a new role for the nucleus in the control of emergent tissue mechanics and architecture.

Simulations predict nuclear jamming in embryonic tissues

To understand the role of varying nuclear volume fraction and nuclear anisotropy (as observed in different zebrafish tissues; Fig. 1) in the emergent physical state of the tissue, we first developed a computational framework that accounts for both cellular and nuclear mechanical interactions (Fig. 2a–c). Building on the active foam description of tissue dynamics[7], we introduced a nucleus within each cell as an individual, soft elliptical particle of fixed size A_N and long and short semiaxes b and a, respectively, that determine the nuclear volume fraction $\phi_N \equiv A_N/A_C$ (where A_C is the cell size) and nuclear anisotropy $\alpha_N \equiv b/a$ (Fig. 2a,b; Methods and Supplementary Notes 1 and 2). Nuclei do not physically interact directly, but rather interact with the cell boundaries on contact, with repulsive interactions between nuclei and cell boundaries defined by a repulsive harmonic potential (Fig. 2c and Methods). To reproduce the experimentally observed nuclear positioning close to the cell centre, we introduced a restoring force for the nucleus to the geometric cell centre (Fig. 2c). Although this effective restoring force enables realistic nuclei dynamics in cells, it does not qualitatively affect our results below.

We first focus on the case of round nuclei ($\alpha_N = 1$). For small nuclear volume fractions, cellular dynamics and tissue architecture are not affected by the presence of nuclei because these rarely interact (Fig. 2d). As the nuclear volume fraction surpasses a value ϕ_N^J of approximately 0.6, all the dynamic and structural measures show that cells start being more constrained (Fig. 2d–f and Supplementary Video 1) and ordered (Fig. 2g–k) as a consequence of nuclear interactions. Both normalized mean squared relative displacement (MSRD; $\mathrm{MSRD}(t)/L_0^2$, where L_0 is the characteristic length scale of the cell size (Methods and Fig. 2d,e)) and the rate of cellular rearrangements (or T1 transition rate; Fig. 2f) decrease strongly as the nuclear volume fraction increases beyond ϕ_N^J (Fig. 2d–f and Supplementary Video 1), indicating a rigidification of the tissue associated with nuclear jamming. Our definition of the nuclear jamming onset ϕ_N^J corresponds to the nuclear volume fraction at which mechanical interaction between nuclei start reducing cellular movements, rather than causing their complete arrest. The specific value of this nuclear jamming volume fraction is independent of the magnitude of active tension fluctuations at cell–cell contacts within the studied range (Extended Data Fig. 1). Very large values of the nuclear volume fraction nearly arrest the system even in the presence of substantial tension fluctuations, indicating that strong nuclear jamming can rigidify a tissue that would otherwise be fluidized by tension fluctuations (Fig. 2e). This is because nuclear jamming obstructs nuclear uncaging behaviour even when cell–cell contacts undergo T1 transitions (Fig. 2f). For values of the nuclear volume fraction leading to nuclear jamming, the emergent tissue mechanics is controlled by the nuclear mechanics rather than by the mechanics of cell–cell contacts if nuclear stiffness E_N is larger than the characteristic stress scale at cell–cell contacts, namely, T_0/L_0 (where T_0 is the average cell–cell contact tension; Methods). Indeed, cell movements and tissue dynamics are unaffected by the presence of nuclei if these are very soft ($E_N < T_0/L_0$), but are strongly affected by stiff nuclei ($E_N \gg T_0/L_0$) at large nuclear volume fractions (Extended Data Fig. 2).

Increasing the nuclear volume fraction above the nuclear jamming value ϕ_N^J also affects the tissue architecture. For high values of nuclear volume fraction, the nuclei's jammed states act as a geometric template for cell shape; consequently, cell shapes become more isotropic and their spatial arrangements, more ordered. The shape factor $\bar{p}$ (namely, the ratio of cell perimeter to square root of the cell area; Methods and Fig. 2g), the topological defect density σ_n^2 (as quantified by the variance in topology distribution; Methods and Fig. 2h,i) and variations in normalized bond lengths s and angles θ (quantified by the standard deviation of normalized bond lengths and angles, namely, $\sigma_{s/\bar{s}}$ and $\sigma_{\theta/\bar{\theta}}$, respectively (Methods and Fig. 2j,k)) decrease as the nuclear volume fraction increases, indicating the formation of a more ordered, crystalline cellular packing structure.

Overall, these results indicate that high nuclear volume fractions for round nuclei lead to nuclear jamming, which overtakes cellular jamming, causing a strong reduction in cell movements, tissue rigidification and ordering of cellular architecture in the tissue.

Nuclear jamming in retina development

To determine if nuclear jamming plays an important role in living tissues, we imaged nuclei and cell boundaries (membranes) in different tissues of various organs at multiple stages of zebrafish development (Fig. 1). Among the imaged tissues, the retina displayed comparatively large nuclei compared with cell size (Figs. 1h and 3a–e), which suggested the possibility of nuclear jamming occurring in this tissue. In vertebrates, out-pocketing of the neural tube gives rise to a single-layered neuroepithelium that defines the initial stages of the retina, with elongated progenitor cells attached to both apical surface and basal lamina[38] (Fig. 3g, 24–36 hours post-fertilization (hpf); Extended Data Figs. 3a and 4). As development progresses, retinal progenitor cells detach from tissue boundaries at approximately 42 hpf and differentiate into retinal neurons[39] (Extended Data Fig. 3b), creating a tissue with more compact cells (Fig. 3g, 55 hpf; Extended Data Fig. 4c,d). The retina is gradually transformed into a layered tissue in which cell bodies of its

https://doi.org/10.1038/s41563-024-01972-3

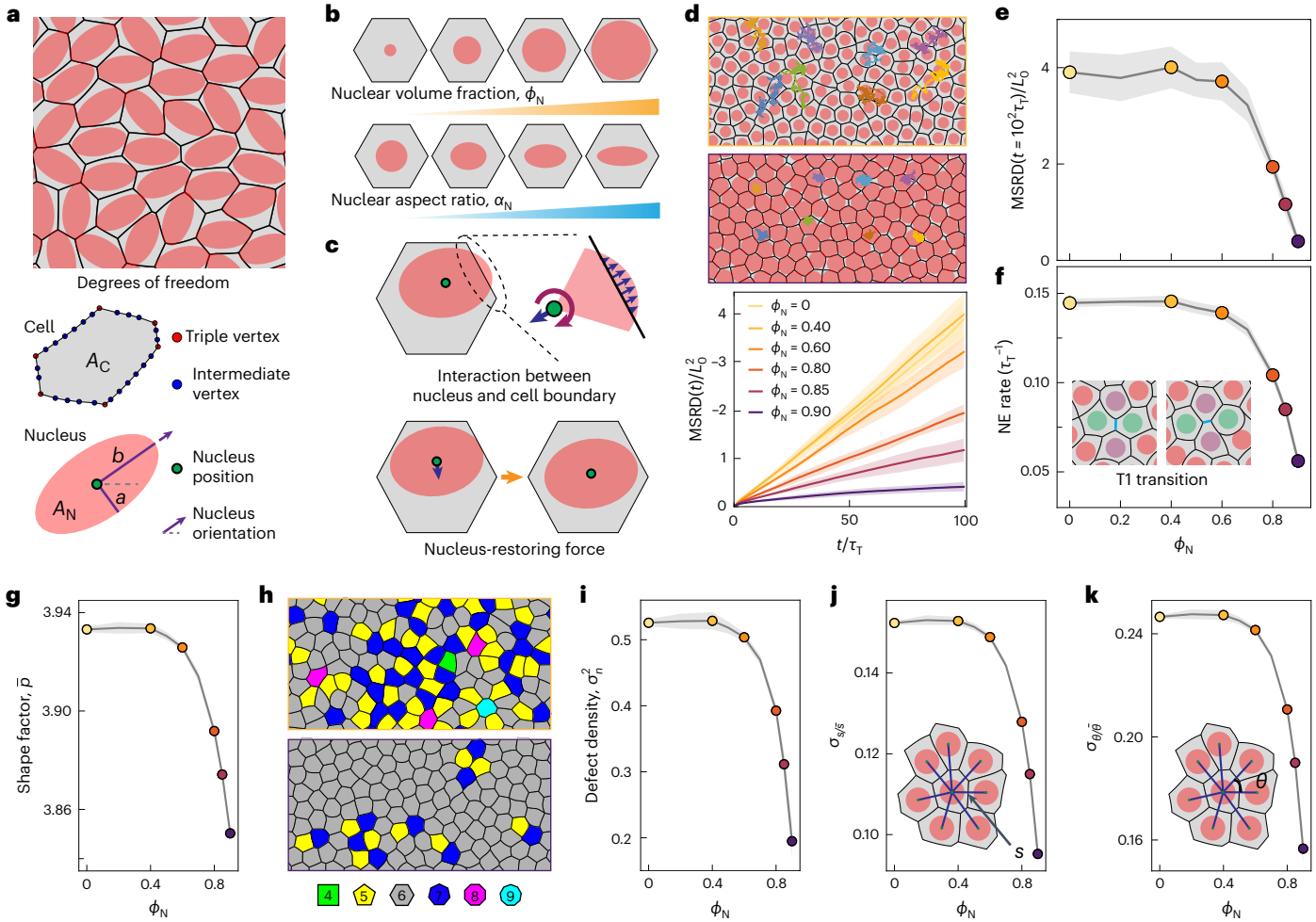

Fig. 2 | Characteristics of nuclear jamming for round nuclei. a, Snapshot of a simulated system configuration showing cells (black borders; grey interior) and nuclei (red), as well as the degrees of freedom for each cell and parameters characterizing the nuclear size and shape. **b**, Schematic with examples of varying nuclear volume fractions ϕ_N and nuclear aspect ratio α_N. **c**, Schematic showing the forces acting on the nuclei (Methods and Supplementary Note 1): force between the nucleus and cell boundary (top), and the effective nucleus-restoring force (down). **d**, Representative cell trajectories for small (top; $\phi_N = 0.4$) and large (down; $\phi_N = 0.9$) volume fractions. MSRD data show a progressive reduction in cell movements for increasing values of nuclear volume fraction ϕ_N. **e**–**k**, Long-time MSRD values (**e**), neighbour-exchange (NE) rate (**f**), shape factor $\bar{p}$ (**g**), defect density σ_n^2 (**i**), snapshot of two system configurations from **i**, colour coded in terms of the number of neighbours) (**h**), standard deviation of normalized bond length $\sigma_{s/\bar{s}}$ (**j**) and standard deviation of normalized bond angle $\sigma_{\theta/\bar{\theta}}$ (**k**) for different nuclear volume fractions. Error bands indicate the standard deviation over $N = 10$ simulations. In all the cases, the magnitude of tension fluctuations was set to $\Delta T/T_0 = 0.25$ (Supplementary Note 2).

five different neuron types are positioned at three morphologically distinct layers from apical to basal: the outer nuclear layer (ONL), inner nuclear layer (INL) and the retinal ganglion cell layer (RGL)[40,41] (Fig. 3g, 55–120 hpf; Extended Data Fig. 4c–g).

To investigate if the retina undergoes nuclear jamming, we first quantified both nuclear volume fraction ϕ_N and nuclear anisotropy α_N as it developed (Fig. 3f). Analysis of cell and nuclear sizes revealed their substantial decrease over time (Fig. 3h and Methods). Although both cell and nuclear sizes decrease, the cell size does so to a larger extent, causing a sharp increase in the nuclear volume fraction as cells detach from tissue surfaces. The nuclear volume fraction in both INL and RGL eventually crosses the predicted onset value of nuclear jamming (Fig. 3i), at approximately 55 hpf, with both layers showing nuclei nearly as large as the cells themselves (Fig. 3d,e). Although the ONL also shows a similar increase, we excluded it from the analysis because of the potentially strong influence from tissue boundaries in the nuclear jamming process. As development further proceeds and the retina progressively reaches its mature organization (72–120 hpf), the nuclear volume fraction in both INL and RGL remains above the predicted nuclear jamming threshold. Altogether, these structural data suggest that the tissue undergoes a nuclear jamming transition at approximately 55 hpf.

To directly assess if the tissue indeed undergoes a nuclear jamming transition, we tracked and quantified three-dimensional (3D) nuclear movements in the INL from 24 to 92 hpf (Fig. 3j–m and Methods). Analysis of the nuclear MSRD showed large, uncaged nuclear movements at 24 hpf (Fig. 3m–o and Supplementary Video 3). MSRD measurements indicated that at 55 hpf, nuclear movements started to be slightly reduced (Fig. 3n–o), although not jammed, in agreement with our predictions that cellular movements start being affected at the nuclear jamming onset (Fig. 3i). At later stages (72–92 hpf), the MSRD showed that nuclear movements are strongly suppressed (Fig. 3m–o and Supplementary Video 4), with nuclei being completely caged by neighbouring nuclei (Fig. 3l–m). These data show that nuclei become physically jammed at a developmental stage between 55 and 72 hpf.

Our simulations indicated that nuclear jamming should result in an emergent tissue stiffness that depends on nuclear stiffness, as it occurs in the jamming of soft elastic particles[21]. To test this, we employed magnetically responsive oil microdroplets to directly measure the stiffness of the nuclear jammed INL tissue in situ, both in control embryos and

https://doi.org/10.1038/s41563-024-01972-3

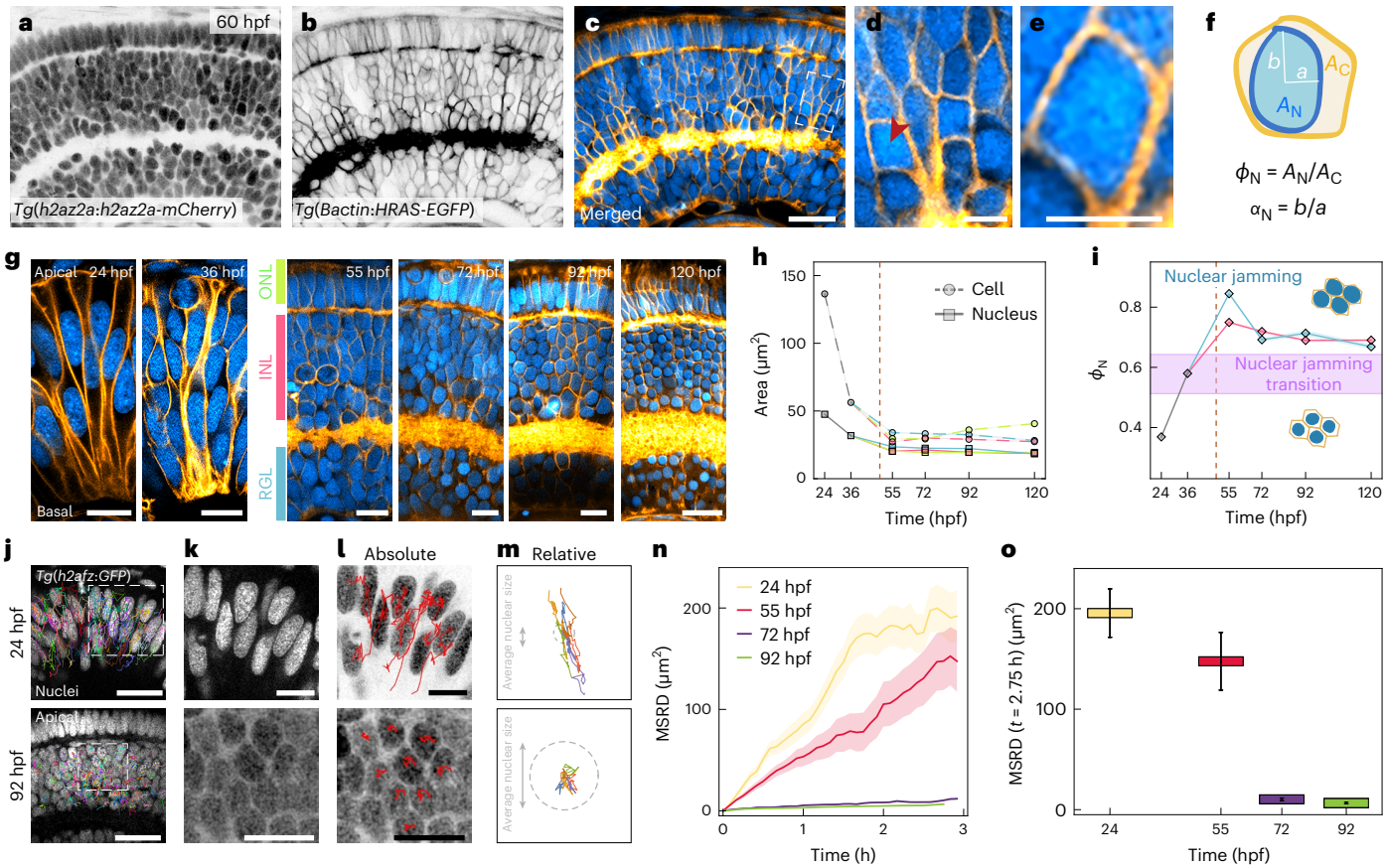

Fig. 3 | Nuclear jamming transition during zebrafish retina development. **a**–**c**, Representative confocal sections of a 60 hpf zebrafish retina (nuclear label, *Tg*(*h2az2a*:*h2az2a-mCherry*) (**a**); membrane label, *Tg*(*Bactin*:*HRAS-EGFP*) (**b**); and merged (**c**)). **d**, Higher-magnification inset of the outlined region in **c**. **e**, High magnification of a cell (arrowhead) in **b**. **f**, Schematic of a retinal cell with the relevant definitions to quantify the nuclear volume fraction ϕ_N and nuclear anisotropy α_N. **g**, Representative confocal sections of the 24, 36, 55, 72, 92 and 120 hpf retina, with distinct layers (from apical to basal; ONL, green; INL, pink; RGL, light blue). **h**, Temporal change in the cell area (A_C; dashed lines) and nuclear area (A_N; solid lines) before cell detachment from tissue boundaries (24 and 36 hpf) and in different layers after detachment (55, 72, 92 and 120 hpf;). **i**, Temporal evolution of nuclear volume fraction in the INL and RGL (Methods). The dashed vertical lines indicate the approximate detachment time (**h**,**i**). The horizontal violet band shows the theoretically predicted volume fraction for nuclear jamming transition (**i**). Statistics (**h** and **i**): 24 hpf ($n = 219, N = 12$), 36 hpf ($n = 319, N = 7$), 55 hpf (ONL: $n = 181, N = 9$; INL: $n = 470, N = 14$; RGL: $n = 195, N = 8$), 72 hpf (ONL: $n = 231, N = 9$; INL: $n = 342, N = 9$; RGL: $n = 275, N = 8$), 92 hpf (ONL: $n = 240, N = 5$; INL: $n = 386, N = 6$; RGL: $n = 150, N = 5$), 120 hpf (ONL: $n = 194, N = 6$; INL: $n = 294, N = 7$; RGL: $n = 151, N = 6$). **j**, Representative confocal sections from time lapses of 24 and 92 hpf zebrafish retina (nuclear label, *Tg*(*H2afz*:*GFP*)) showing the trajectories of tracked nuclei for a duration of 3 h (24 hpf ($n = 90$), 92 hpf ($n = 260$)). **k**, Higher-magnification insets of the outlined regions in **j**. **l**,**m**, Representative examples of absolute (**l**) and relative (**m**) tracks. **n**, MSRD measurements. Statistics: 24 hpf: $n = 5{,}148, N = 11$; 55 hpf: $n = 3{,}777, N = 6$; 72 hpf: $n = 6{,}359, N = 8$; 92 hpf: $n = 3{,}564, N = 5$. Error bands: standard error of the mean (s.e.m.). **o**, Final MSRD value for each developmental stage (24 hpf: $n = 111, N = 11$; 55 hpf: $n = 100, N = 6$; 72 hpf: $n = 174, N = 8$; 92 hpf: $n = 297, N = 5$). Error bands: s.e.m. Scale bars, 20 μm (**a**–**c**), 5 μm (**d** and **e**), 10 μm (**g**), 20 μm (**j**), 10 μm (**k** and **l**). n = cells per nuclei, N = embryos.

in embryos with overexpressed levels of lamin A[42] (Methods), a type-V intermediate filament lamin protein of the nuclear lamina known to control nuclear stiffness[30,43]. After inserting the droplets in the INL of 72 hpf embryos (Fig. 4a and Methods), we applied a controlled, uniform magnetic field to deform the droplet and apply a known stress to the tissue (Fig. 4b and Methods), as previously established[6,44,45]. Only when the applied stresses in the embryos with overexpressed lamin A were approximately twice as large as those applied in control embryos, we could observe similar levels of droplet deformation, or strain (Fig. 4c), indicating that the INL of embryos with higher levels of lamin A is substantially stiffer. Quantification of the effective tissue stiffness showed that the INL of embryos with overexpressed lamin A is considerably stiffer than in control embryos (Fig. 4d), indicating that the emergent tissue stiffness depends on nuclear stiffness (lamin A level; Fig. 4e), as expected for a nuclear jammed state in which nuclei mechanically interact with each other (Supplementary Note 4 and Supplementary Fig. 3). These results are consistent with recent data showing that an increase in nuclear stiffness reduces cellular movements in the zebrafish retina[46]. Altogether, our structural measurements, analysis of cellular movements and mechanical measurements and perturbations indicate that the retina undergoes a nuclear jamming transition between 55 and 72 hpf, with cellular movements strongly suppressed and the tissue stiffness controlled by nuclear stiffness in the nuclear jammed state.

Ordering of cellular packings in the nuclear jammed retina

Our theoretical predictions indicated that cellular packings should become progressively ordered in nuclear jammed states (Fig. 2g–k), especially for round nuclei. Although both cell and nuclear anisotropies, as well as shape factors, were large at early developmental stages of the retina, when the tissue features a neuroepithelial architecture (Extended Data Figs. 3a,b and 4a,b) and the nuclei are unjammed (Fig. 3j–o), they decreased progressively over time as cells detached from tissue boundaries and continued doing so after that (Fig. 5a). At 55 hpf, when cellular movements started to be slightly reduced

https://doi.org/10.1038/s41563-024-01972-3

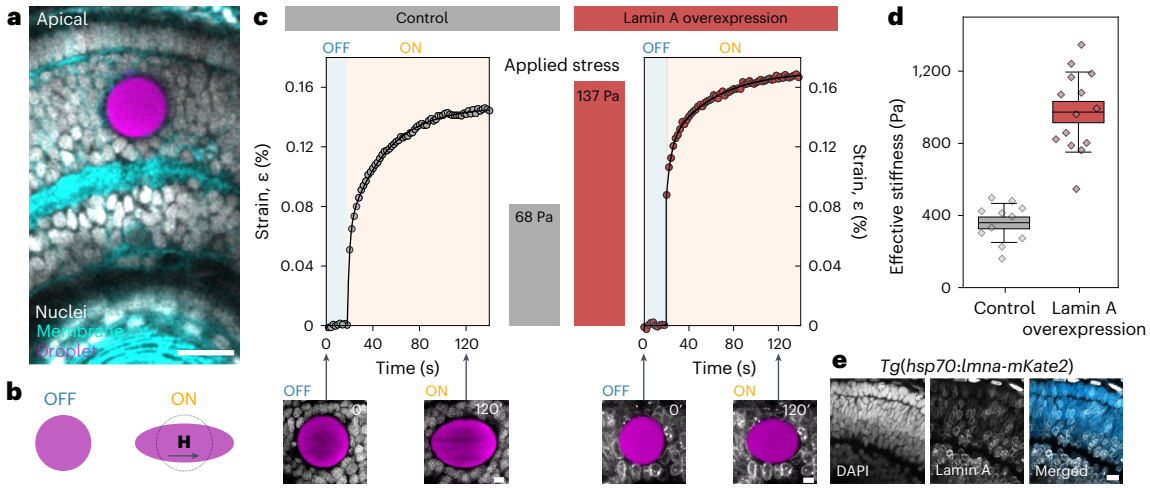

Fig. 4 | Retina INL tissue mechanics is controlled by nuclear mechanics. **a**, Representative confocal section of a ferrofluid oil droplet (magenta) in the INL region of *Tg*(*Bactin*:*HRAS-EGFP*); *Tg*(*h2az2a*:*h2az2a-mCherry*) zebrafish embryonic retina (membranes, cyan; nuclei, white). Scale bar, 20 µm. **b**, Schematic of a droplet before actuation (magnetic field OFF) and after the application of a uniform magnetic field **H** (magnetic field ON). The dashed lines indicate the undeformed droplet. **c**, Temporal evolution of strain ε during magnetic actuation in control embryos (*Tg*(*h2az2a*:*h2az2a-mCherry*); grey) and embryos with overexpressed lamin A (*Tg*(*hsp70*:*lmna-mKate2*); red) at 72 hpf. Experimental data points (grey/red) and fit (black line) are shown. The snapshots of droplet (magenta) shape before (0′) actuation and 120 min after actuation are shown for control embryos (*Tg*(*h2az2a*:*h2az2a-mCherry*); nuclei, white) and for embryos with overexpressed lamin A (*Tg*(*hsp70*:*lmna-mKate2*); lamin A, white). Scale bars, 5 µm. **d**, Measured effective stiffness in control embryos and in embryos with overexpressed lamin A. Statistics: average (centre horizontal line), s.e.m. (filled box) and standard deviation (error bar) are indicated. $N = 11$ (control) and $N = 14$ (lamin A overexpression) independent samples. **e**, Confocal section of a 72 hpf retina of a *Tg*(*hsp70*:*lmna-mKate2*) embryo post-heat-shock showing nuclei (DAPI staining, left), lamin A (centre) and merged (right) images (Methods), indicating the presence of lamin A surrounding the nuclei in the jammed INL tissue. Scale bar, 10 µm.

by nuclear interactions at the onset of nuclear jamming (Fig. 3n,o), nuclei were still fairly anisotropic (Fig. 5a). Eventually, as development progressed, both cell bodies and nuclei displayed more compact shapes, with nuclei becoming nearly round in both INL and RGL (Fig. 5a; $\alpha_N \simeq 1.2$ at 120 hpf). To understand if this progressive rounding of the nuclei in the nuclear jammed state affected the order of cellular packings, we analysed the structure of cellular packings in the INL. From the network spanned by connections between the centres of the nearest-neighbouring nuclei (Fig. 5b), we obtained the lengths between a nucleus and its nearest neighbours (bond lengths; Methods) as well as the angles between the nearest neighbours (bond angles; Methods) at both 55 and 120 hpf (Fig. 5b–d). We observed that the variations in both bond lengths (Fig. 5c) and angles (Fig. 5d) showed substantial reductions from 55 to 120 hpf. These results indicate that the cellular packing structure of the INL becomes more ordered as the jammed nuclei become rounder, with cells forming a nearly crystalline arrangement at 120 hpf, as predicted by our simulations. This is consistent with the formation of the precise and almost crystalline ordering of the neighbouring retinal cell types known as retinal mosaics, which is proposed to ensure the even distribution of retinal cells and consequently tissue functionality[4,41].

Nuclear jamming in brain tissues

Beyond eye development, we examined other neural tissues to understand if a similar behaviour was observed. In particular, we compared the characteristics of cell and nuclear sizes and shapes in the midbrain (MB) at early (18 hpf) and later (92 hpf) stages of brain development in zebrafish[47]. At 18 hpf, the MB architecture is that of a pseudostratified neuroepithelium (Fig. 5e–g). After cells detach from the tissue boundaries, the dorsal part of the MB later gives rise to the optic tectum (OT), a tissue that coordinates eye movement and visual processing in zebrafish and other amphibians[48] (Fig. 5h–j). Our analysis showed that both cell and nuclear sizes, as well as their aspect ratios, strongly decreased from their values in the MB (18 hpf) to those measured in the OT (92 hpf), with the cell size and aspect ratio decreasing more than the nuclei's (Extended Data Fig. 5a,b), as was the case in the retina. Although the measured nuclear volume fraction is below the nuclear jamming threshold in the MB (Extended Data Fig. 5c), it is larger than the threshold in the OT, suggesting that the tissue underwent a nuclear jamming transition during or after cells detached from the tissue boundaries. In addition, the shape factor of both cells and nuclei strongly decreased from the MB to the OT (Extended Data Fig. 5d), as cells became more compact and nuclei nearly round (Fig. 5j). These data are consistent with nuclear jamming also occurring in these brain tissues, with very similar structural characteristics as those reported above for retina development, including the more ordered cell packings (Fig. 5j) associated with the jamming of round nuclei.

Phase diagram of nuclear jamming

To understand the different phases of nuclear jamming, we computed the phase diagram as a function of the two relevant parameters in the system, namely, the nuclear volume fraction ϕ_N and nuclear anisotropy α_N (Supplementary Note 3 and Supplementary Video 2 show details on the role of nuclear shape anisotropy). For small values of nuclear volume fraction, the system displays cellular jamming but not nuclear jamming (Fig. 5m). As the nuclear volume fraction increases over an anisotropy-dependent volume fraction $\phi_N^J(\alpha_N)$, the system undergoes either a transition to jammed isotropic nuclei for small (or no) nuclear anisotropy or a transition to jammed anisotropic nuclei without strongly affecting the cell shapes. Large nuclear anisotropy and volume fraction levels lead to strong jamming of the anisotropic nuclei that substantially deform the cell shapes, causing local nematic ordering in the system.

Plotting the measured developmental trajectory for the retina (INL) in the phase space (Fig. 5m), we observe that cells in the retina first start to undergo nuclear jamming with highly anisotropic nuclei at 55 hpf and subsequently decrease their nuclear aspect ratio maintaining the nuclear jammed state. This progressive reduction in nuclear anisotropy (nuclear rounding) in a nuclear jammed state causes the observed ordering of cellular packings, eventually generating a nearly crystalline structure. Since nuclear jamming causes nuclei to be more

https://doi.org/10.1038/s41563-024-01972-3

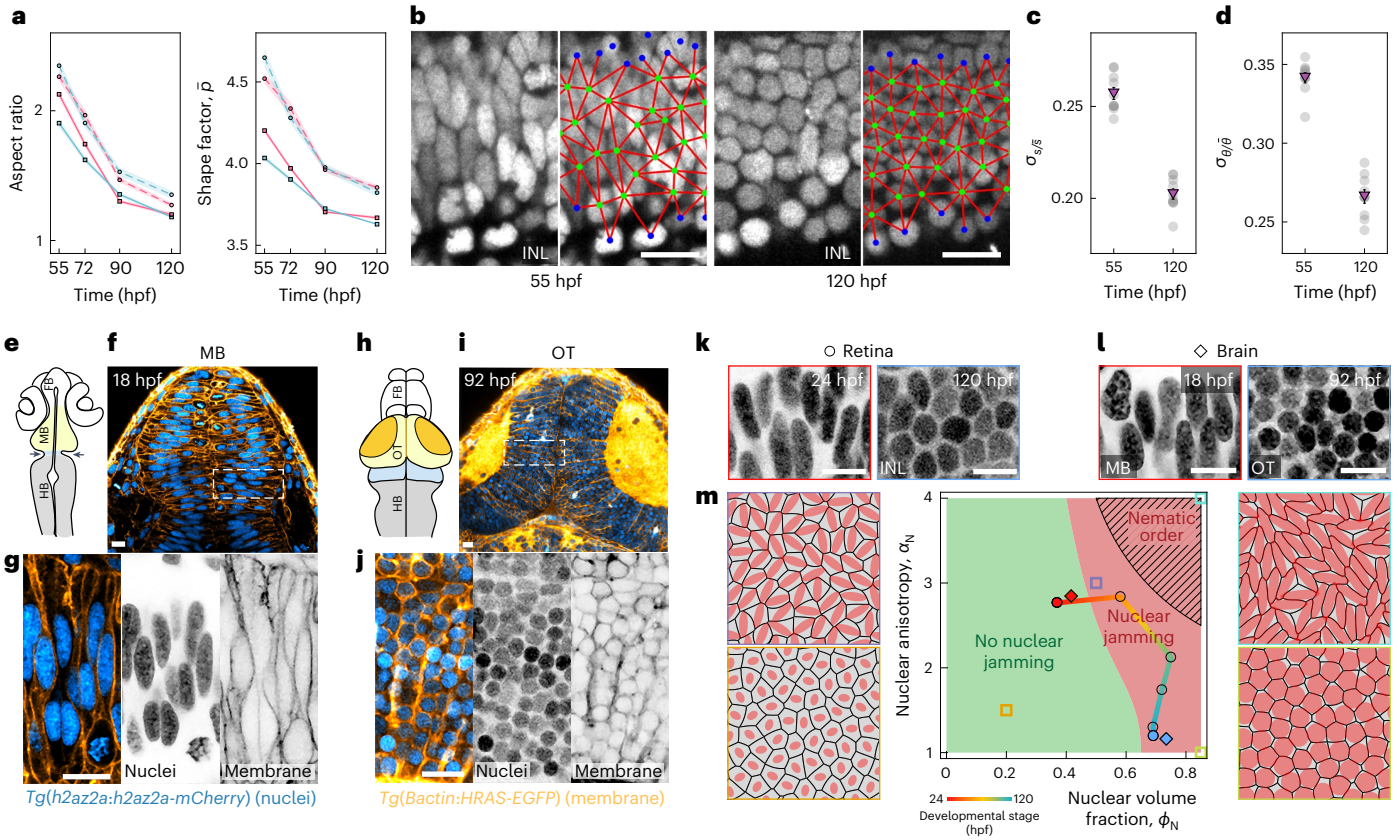

Fig. 5 | Nuclear jamming in retina and brain tissues leads to ordering of cellular packings. a, Temporal evolution of the aspect ratio (left) and shape factor (right) for cells (dashed lines) and nuclei (solid lines) in the INL and RGL. Statistics: 55 hpf (INL: $n = 470$, $N = 14$; RGL: $n = 195$, $N = 8$), 72 hpf (INL: $n = 342$, $N = 9$; RGL: $n = 275$, $N = 8$), 92 hpf (INL: $n = 386$, $N = 6$; RGL: $n = 150$, $N = 5$), 120 hpf (INL: $n = 294$, $N = 7$; RGL: $n = 151$, $N = 6$). Error bands: s.e.m. **b**, Confocal sections of the INL showing the nuclei (left) and network (red) connecting the geometrical centres (green; blue indicates those at the INL boundary) of nearest neighbours (right; overlaid) at 55 and 120 hpf. Scale bars, 20 µm. **c**,**d**, Variation in distances s (**c**) and angles θ (**d**) of the nearest neighbours (Methods). Statistics: $N = 10$ embryos. **e**, Schematic of an 18 hpf zebrafish brain; MB (light yellow), hindbrain (HB, grey), forebrain (FB, white), arrowheads (MB–HB boundary, blue). **f**, Representative confocal section of an 18 hpf MB (nuclear label, *Tg*(*h2az2a:h2az2a-mCherry*); membrane label, *Tg*(*Bactin:HRAS-EGFP*)). **g**, Higher-magnification insets of the outlined region in **f**. **h**, Schematic of a 92 hpf zebrafish brain showing that the MB developed into the optic tectum (OT, light yellow). **i**, Representative confocal section of a 92 hpf OT (same markers as in **f**). **j**, Higher-magnification insets of the outlined region in **i**. **k**,**l**, Representative confocal sections of nuclei in the retina (24 hpf, red; 120 hpf, blue) (**k**) and brain (18 hpf, red; 92 hpf, blue) (**l**). **m**, Predicted phase space for varying the values of the nuclear volume fraction ϕ_N and nuclear anisotropy α_N. Representative simulation snapshots for limiting phases are shown (orange, no nuclear jamming; green, nuclear jamming for round nuclei; violet, nuclear jamming for anisotropic nuclei; cyan, local nematic domain). The continuous line with graded colour shows the developmental trajectory of the retina from 24 hpf (red circle) to 120 hpf (blue circle). The locations of MB in the phase space at 18 hpf (red diamond) and after developing into the OT (92 hpf; blue diamond) are also shown. Scale bars, 10 µm.

deformed due to their mechanical interactions (Supplementary Note 4 and Supplementary Fig. 3), the progressive rounding of nuclei as the retina forms is probably developmentally controlled. This suggests that the emergent cellular crystalline order is the combined result of nuclear jamming and programmed nuclear rounding. Although we lack an exhaustive developmental trajectory for brain tissues, the initial MB state (18 hpf) and final OT state (92 hpf) are essentially located in the same region of the phase space as the initial and final stages of retina development, suggesting that different neural tissues may follow similar developmental trajectories as they undergo nuclear jamming.

Outlook

Understanding the role of subcellular structures in the control of the emergent tissue physical state and architecture is essential to connect relevant biological processes occurring at different scales during embryonic development. Our computational and experimental results show that nuclei play an important role in the emergent physical state of the tissue during organ formation in vertebrates.

We introduced nuclei in the active foam description of tissues[7], enabling studies of the interplay between the nuclear properties and the cell and tissue structure and dynamics. In the absence of nuclei, previous models predicted the existence of rigidity transitions in multicellular systems[7,24,27,29]. By controlling the nuclear volume fraction, cells can change the emergent properties of the tissue from being controlled by the mechanics of cell–cell contacts to the mechanics of the nuclei, as well as change the structure of cellular packings, directly linking the physical properties of the nucleus to the physical state of the tissue. Our theoretical description is clearly a simplification of the real situation, especially in the treatment of nuclei, ignoring nuclear shape deformation and volume changes, complex nuclear mechanics, friction between the nucleus and cell surface, potential changes of the model parameters during development and 3D nature of the tissue. Although our simple two-dimensional (2D) model can capture the existence of the nuclear jamming transition and several key features, it is probable that the precise volume fraction at which nuclear jamming occurs depends on all these factors to different degrees. Future studies will identify how each of these factors affect nuclear jamming and its properties.

Our structural measurements and quantification of cell movements, as well as our in vivo measurements of tissue stiffness and its

perturbation in embryos with overexpressed lamin A, show that nuclear jamming occurs during retina development. Altogether, our observations indicate that nuclei are unjammed at 24 hpf; then, nuclei start to mechanically interact at approximately 48 hpf, with these interactions causing nuclear movements to start decreasing in the INL at 55 hpf. Finally, the INL undergoes a nuclear jamming transition between 55 and 72 hpf. Although all our data are consistent with nuclei driving the observed jamming transition, the potential effects of nuclear mechanics or shape on other cellular processes[49,50], including the cytoskeleton, could also contribute to the observed changes in tissue mechanics and dynamics. It will be interesting to dissect how nuclear mechanotransduction in crowded environments affects the reported nuclear jammed states. Beyond the retina, the structural measurements in brain tissues closely mirror those in the retina, suggesting that the nuclear jamming transition may occur in multiple neural tissues. To clearly assess if nuclear jamming occurs in other tissues, direct mechanical measurements and quantifications of cellular dynamics will be necessary.

In nuclear jammed states, we observed that the structure of cellular packings becomes more ordered, as theoretically predicted, resembling the nearly crystalline cellular packings in the adult functional eye. Nuclear jamming, thus, provides a different cell-ordering mechanism than those reported for epithelial tissues[3,4]. Moreover, our direct mechanical measurements show that in the nuclear jammed state, high nucleus stiffness in embryos overexpressing lamin A translates into a stiffer tissue, which could also play a functional role by providing further mechanical integrity to the tissue.

These results highlight the importance of nuclear volume fraction in the control of the emergent tissue physical state and architecture, and provide a direct connection between the supracellular state and a subcellular organelle. Future studies will reveal if nuclear jamming occurs in other organs and species, as well as establish its functional roles.

Online content

Any methods, additional references, Nature Portfolio reporting summaries, source data, extended data, supplementary information, acknowledgements, peer review information; details of author contributions and competing interests; and statements of data and code availability are available at https://doi.org/10.1038/s41563-024-01972-3.

References

1. Heisenberg, C. P. & Bellaïche, Y. Forces in tissue morphogenesis and patterning. *Cell* **153**, 948–962 (2013).
2. Guillot, C. & Lecuit, T. Mechanics of epithelial tissue homeostasis and morphogenesis. *Science* **340**, 1185–1189 (2013).
3. Cohen, R. et al. Mechanical forces drive ordered patterning of hair cells in the mammalian inner ear. *Nat. Commun.* **11**, 5137 (2020).
4. Salbreux, G., Barthel, L. K., Raymond, P. A. & Lubensky, D. K. Coupling mechanical deformations and planar cell polarity to create regular patterns in the zebrafish retina. *PLoS Comput. Biol.* **8**, e1002618 (2012).
5. Kim, S., Cassidy, J. J., Yang, B., Carthew, R. W. & Hilgenfeldt, S. Hexagonal patterning of the insect compound eye: facet area variation, defects, and disorder. *Biophys. J.* **111**, 2735–2746 (2016).
6. Mongera, A. et al. A fluid-to-solid jamming transition underlies vertebrate body axis elongation. *Nature* **561**, 401–405 (2018).
7. Kim, S., Pochitaloff, M., Stooke-Vaughan, G. A. & Campàs, O. Embryonic tissues as active foams. *Nat. Phys.* **17**, 859–866 (2021).
8. Petridou, N. I., Grigolon, S., Salbreux, G., Hannezo, E. & Heisenberg, C.-P. Fluidization-mediated tissue spreading by mitotic cell rounding and non-canonical Wnt signalling. *Nat. Cell Biol.* **21**, 169–178 (2019).
9. Lenne, P. F. & Trivedi, V. Sculpting tissues by phase transitions. *Nat. Commun.* **13**, 664 (2022).
10. Atia, L. et al. Geometric constraints during epithelial jamming. *Nat. Phys.* **14**, 613–620 (2018).
11. Parada, C. et al. Mechanical feedback defines organizing centers to drive digit emergence. *Dev. Cell* **57**, 854–866.e6 (2022).
12. Shelton, E. R. et al. Stress-driven tissue fluidization physically segments vertebrate somites. Preprint at *BioRxiv* https://doi.org/10.1101/2021.03.27.437325 (2021).
13. Lawton, A. K. et al. Regulated tissue fluidity steers zebrafish body elongation. *Development* **140**, 573–582 (2013).
14. Bénażeraf, B. et al. A random cell motility gradient downstream of FGF controls elongation of an amniote embryo. *Nature* **466**, 248–252 (2010).
15. Schotz, E. M., Lanio, M., Talbot, J. A. & Manning, M. L. Glassy dynamics in three-dimensional embryonic tissues. *J. R. Soc. Interface* **10**, 20130726–20130726 (2013).
16. Yanagida, A. et al. Cell surface fluctuations regulate early embryonic lineage sorting. *Cell* **185**, 777–793.e20 (2022).
17. Oswald, L., Grosser, S., Smith, D. M. & Käs, J. A. Jamming transitions in cancer. *J. Phys. D: Appl. Phys.* **50**, 483001–483018 (2017).
18. Palamidessi, A. et al. Unjamming overcomes kinetic and proliferation arrest in terminally differentiated cells and promotes collective motility of carcinoma. *Nat. Mater.* **80**, 1252–1263 (2019).
19. Kang, W. et al. A novel jamming phase diagram links tumor invasion to non-equilibrium phase separation. *iScience* **24**, 103252 (2021).
20. Campàs, O., Noordstra, I. & Yap, A. S. Adherens junctions as molecular regulators of emergent tissue mechanics. *Nat. Rev. Mol. Cell Biol*. 252–269 (2023).
21. Bonn, D., Denn, M. M., Berthier, L., Divoux, T. & Manneville, S. Yield stress materials in soft condensed matter. *Rev. Mod. Phys.* **89**, 15 (2017).
22. Angelini, T. E. et al. Glass-like dynamics of collective cell migration. *Proc. Natl Acad. Sci. USA* **108**, 4714–4719 (2011).
23. Park, J.-A. et al. Unjamming and cell shape in the asthmatic airway epithelium. *Nat. Mater.* **14**, 1040–1048 (2015).
24. Krajnc, M. Solid–fluid transition and cell sorting in epithelia with junctional tension fluctuations. *Soft Matter* **16**, 3209–3215 (2020).
25. Krajnc, M., Dasgupta, S., Ziherl, P. & Prost, J. Fluidization of epithelial sheets by active cell rearrangements. *Phys. Rev. E* **98**, 022409 (2018).
26. Boromand, A., Signoriello, A., Ye, F., O'Hern, C. S. & Shattuck, M. D. Jamming of deformable polygons. *Phys. Rev. Lett.* **121**, 248003 (2018).
27. Bi, D., Lopez, J. H., Schwarz, J. M. & Manning, M. L. A density-independent rigidity transition in biological tissues. *Nat. Phys.* **11**, 1074–1079 (2015).
28. Bi, D., Yang, X., Marchetti, M. C. & Manning, M. L. Motility-driven glass and jamming transitions in biological tissues. *Phys. Rev. X* **6**, 021011 (2016).
29. Farhadifar, R., Röper, J.-C., Aigouy, B., Eaton, S. & Jülicher, F. The influence of cell mechanics, cell-cell interactions, and proliferation on epithelial packing. *Curr. Biol.* **17**, 2095–2104 (2007).
30. Lammerding, J. Mechanics of the nucleus. *Compr. Physiol.* **1**, 783–807 (2011).
31. Jevtić, P., Edens, L. J., Vuković, L. D. & Levy, D. L. Sizing and shaping the nucleus: mechanisms and significance. *Curr. Opin. Cell Biol.* **28**, 16–27 (2014).
32. Chow, K.-H., Factor, R. E. & Ullman, K. S. The nuclear envelope environment and its cancer connections. *Nat. Rev. Cancer* **12**, 196–209 (2012).
33. Dutta, S., Djabrayan, N. J.-V., Torquato, S., Shvartsman, S. Y. & Krajnc, M. Self-similar dynamics of nuclear packing in the early *Drosophila* embryo. *Biophys. J.* **117**, 743–750 (2019).
34. Donoughe, S., Hoffmann, J., Nakamura, T., Rycroft, C. H. & Extavour, C. G. Nuclear speed and cycle length co-vary with local density during syncytial blastoderm formation in a cricket. *Nat. Commun.* **13**, 3889 (2022).

35. Kaiser, F. et al. Mechanical model of nuclei ordering in *Drosophila* embryos reveals dilution of stochastic forces. *Biophys. J.* **114**, 1730–1740 (2018).
36. Azizi, A. et al. Nuclear crowding and nonlinear diffusion during interkinetic nuclear migration in the zebrafish retina. *eLife* **9**, e58635 (2020).
37. Hecht, S. et al. Mechanical constraints to cell-cycle progression in a pseudostratified epithelium. *Curr. Biol.* **32**, 2076–2083.e2 (2022).
38. Fuhrmann, S. Chapter three—eye morphogenesis and patterning of the optic vesicle. *Curr. Top. Dev. Biol.* **93**, 61–84 (2010).
39. Agathocleous, M. & Harris, W. A. From progenitors to differentiated cells in the vertebrate retina. *Annu Rev. Cell Dev. Biol.* **25**, 45–69 (2009).
40. Dowling, J. E. *The Retina: An Approachable Part of the Brain, Revised Edition* (Harvard Univ. Press, 2012).
41. Galli-Resta, L. et al. The genesis of retinal architecture: an emerging role for mechanical interactions? *Prog. Retin. Eye Res.* **27**, 260–283 (2008).
42. Amini, R. et al. Amoeboid-like migration ensures correct horizontal cell layer formation in the developing vertebrate retina. *eLife* **11**, e76408 (2022).
43. Lammerding, J. et al. Lamins A and C but not lamin B1 regulate nuclear mechanics. *J. Biol. Chem.* **281**, 25768–25780 (2006).
44. Serwane, F. et al. In vivo quantification of spatially varying mechanical properties in developing tissues. *Nat. Methods* **14**, 181–186 (2017).
45. Mongera, A. et al. Mechanics of the cellular microenvironment as probed by cells in vivo during zebrafish presomitic mesoderm differentiation. *Nat. Mater.* **22**, 135–143 (2023).
46. Maia-Gil, M. et al. Nuclear deformability facilitates apical nuclear migration in the developing zebrafish retina. Preprint at *bioRxiv* https://doi.org/10.1101/2024.04.04.588091 (2024).
47. Mueller, T. & Wullimann, M. *Atlas of Early Zebrafish Brain Development: A Tool for Molecular Neurogenetics* (Academic Press, 2016).
48. Suzuki, D. G., Pérez-Fernández, J., Wibble, T., Kardamakis, A. A. & Grillner, S. The role of the optic tectum for visually evoked orienting and evasive movements. *Proc. Natl Acad. Sci. USA* **116**, 15272–15281 (2019).
49. Lomakin, A. J. et al. The nucleus acts as a ruler tailoring cell responses to spatial constraints. *Science* **370**, eaba2894 (2020).
50. Venturini, V. et al. The nucleus measures shape changes for cellular proprioception to control dynamic cell behavior. *Science* **370**, eaba2644 (2020).

Methods

Zebrafish husbandry, transgenic lines fish lines and experimental manipulations

Zebrafish (*Danio rerio*) were maintained as previously described[51]. Experiments were performed following all the ethical regulations and according to protocols approved by the European Union directive 2010/63/EU as well as the German Animal Welfare Act. Since the sex of zebrafish embryos and larvae at the studied stages cannot be distinguished, sex-specific experiments were not necessary. For the ubiquitous labelling of cell membranes, we either used *Tg*(*Bactin*:*HRAS-EGFP*)^{vu119} (ref. 52) or *Tg*(*actb2*:*MA-mCherry2*)^{hm29} (ref. 53). For ubiquitous nuclear labelling, we either used *Tg*(*h2az2a*:*h2az2a-mCherry*)^{tud7} (ref. 54) or *Tg*(*h2afz*:*GFP*)^{kca6} (ref. 55). To overexpress the lamin A levels, we used *Tg*(*hsp70*:*lmna-mKate2*) (ref. 42), a heat-shock promoter (hsp70)-driven transgene. To ensure enough overexpression of lamin A at 72 hpf, we heat-shocked the manually dechorionated zebrafish embryos for 30 min at 39 °C at both 30 and 55 hpf.

Theoretical description

We extended the previously published active foam computational framework for tissue dynamics to include nuclei. Tangential and normal forces at cell boundaries (accounting for cortical tension and adhesion, as well as osmotic pressure), nucleus–cell boundary interaction forces and a nucleus-restoring force towards the geometric cell centre were implemented (Fig. 2c and Supplementary Note 1). The effective interaction potential between the nuclei and cell boundaries was approximated as a repulsive harmonic potential, with the resulting repulsive force being along the normal direction of the cell boundary at every point of the interaction. The total repulsive force acting on each nucleus is the integral of the distributed interaction forces along the cell boundary. The restoring force of the nucleus to the cell centre is modelled as a linear force acting on the nucleus centre and pulling it towards the geometric cell centre (Supplementary Note 1).

Simulations

All the simulations included $N = 256$ cells in a periodic square box. An initial configuration consisting of a random Poisson–Voronoi tessellation was first generated in a periodic square box and the system was allowed to relax for $10\tau_T$ before sampling the data points. Confluency (no spaces between cells) was enforced for all the simulations. The governing equations are non-dimensionalized with characteristic scales (Supplementary Note 2), and they are numerically integrated using the Euler method and the Euler–Maruyama method with a time step of $\Delta t = 0.01\tau_R$, where τ_R is the vertex relaxation timescale that is the smallest characteristic timescale in the system (Supplementary Note 2).

Analysis of simulated cell trajectories and MSRD

Cell trajectories were computed by tracking the centre positions of all the cells for each time point. To quantify the cell movements, we computed the MSRD, as previously done[6]. For each cell trajectory $\mathbf{r}_i(t)$, the nearest neighbour at an initial time point was first identified and a relative distance vector between cell i and its nearest-neighbour cell j, that is, $\mathbf{r}_{ij}(t) = \mathbf{r}_i(t) - \mathbf{r}_j(t)$, was computed accordingly. We computed the MSRD of a given cell i as $\mathrm{MSRD}_i(t) = (\mathbf{r}_{ij}(t) - \mathbf{r}_{ij}(0))^2$, and the MSRD values were averaged over all the cells as well as all the initial time points. The MSRD values were normalized by the characteristic length scale of cell size L_0.

Analysis of tissue structure in simulations

To investigate structural changes in the simulated tissues, we used four different structure measures: (1) shape factor, (2) defect density, (3) bond length variation and (4) bond angle variation. The shape factor $\bar{p}$ was defined as the mean of the ratio of cell perimeter P_i to the square root of the cell area A_i, namely,

$$\bar{p} = \left\langle P_i/\sqrt{A_i} \right\rangle. \tag{1}$$

This measure quantifies the degree of anisotropy in cell shape and was previously used to identify density-independent rigidity transition[23,27]. The defect density σ_n^2 was defined as the variance in topology distribution and it quantifies the number density of cells that have a number of neighbours different from six. With n_i being number of neighbours for cell i, the defect density can be computed as

$$\sigma_n^2 = \left\langle (n_i - 6)^2 \right\rangle. \tag{2}$$

A network structure of a given tissue configuration (cellular packings) was constructed by connecting bonds between all the cells with their neighbours. The bond length s is the length of the line connecting a cell and a nearest neighbour (Fig. 2j, inset), and the bond angle θ is the angle between the two adjacent nearest neighbours of a given cell (Fig. 2k, inset). The standard deviation of normalized bond length $\sigma_{s/\bar{s}}$ and that of normalized bond angle $\sigma_{\theta/\bar{\theta}}$ were accordingly computed to quantify the degree of variation in these measures.

In 2D confluent systems, the ground state of the monodisperse cell packing exhibits a crystalline hexagonal order. This situation corresponds to a minimum shape factor for the confluence condition, zero defect density and zero variation in the bond length and bond angle, respectively. Hence, any deviation from the ground-state structural measures quantifies the degree of structural disorder in the system.

To quantify the local nuclei alignment, we defined the local nematic order parameter as follows. For a given pair of neighbouring cell i and cell j with the corresponding nuclei orientation θ_i and θ_j, their nuclei alignment is computed as $\cos 2(\theta_i - \theta_j)$, where the value of 1 and −1 correspond to the same orientation and perpendicular orientation of neighbouring nuclei, respectively. The local nematic order parameter P_{LN} is equal to the mean of the alignment measure over all the neighbouring pairs of cells, namely,

$$\bar{P}_{\mathrm{LN}} = \langle \cos 2(\theta_i - \theta_j) \rangle. \tag{3}$$

The local nematic parameter value is positive when neighbouring nuclei align in the same direction, whereas the random orientation of nuclei corresponds to zero.

To compute the mean number of contacts between the nuclei and cell boundaries $\bar{z}_N$, all the cell boundaries of a given cell that exert a repulsive force to its nucleus were counted as contacting the cell boundaries. Taking the average of the number of contacting cell boundaries over all the cells, we can quantify the degree of interaction between the nuclei and cell boundaries.

Imaging of retina and brain tissue structure

Embryos were manually dechorionated and anaesthetized in 0.02% tricane methane sulfonate (MS-222; Sigma-Aldrich) in E3 medium for approximately 15 min. The medium was supplemented with 0.2 mM 1-phenyl-2-thiourea (PTU) (Sigma-Aldrich) from 8 ± 1 hpf onwards to prevent pigmentation. Immobilized embryos were then placed in 1% low-melting-point agarose (in E3) in glass-bottom dishes (MatTek). Samples were mounted for lateral or dorsal imaging for retina and brain samples, respectively. The dishes were filled with E3 medium containing MS-222 (0.02%) and PTU (0.2 mM, Sigma-Aldrich) and imaged at room temperature. Samples from 18 to 72 hpf were imaged on a confocal laser scanning microscope (Zeiss, LSM780) using the ×40/1.2 C-Apochromat water-immersion objective (Zeiss). The Z stacks were recorded with 0.44 µm confocal sectioning. For later developmental stages with high tissue thickness (72–120 hpf), we used a multiphoton confocal laser scanning microscope (two-photon inverted microscope; Leica, SP8) with a ×40/1.1 HC PL IRAPO, water-immersion objective (Leica). The Z stacks were recorded with 0.5 µm optical sectioning.

Imaging and tracking nuclear movements

Imaging of 24, 72 and 92 hpf embryos was performed with a confocal laser scanning microscope (Zeiss, LSM 980) using the ×40/1.1 C-Apochromat water-immersion objective (Zeiss). The image stacks spanned the entire volume of each retina (80–120 µm, depending on the developmental stage), with a *Z*-step size of 0.75–1.00 µm. The 3D confocal volumes were acquired at 150 s, 5 min and 15 min intervals, for the 24, 72 and 92 hpf retina, respectively, and for at least 3 h each. Live imaging of the 55 hpf embryos was carried out on a Zeiss lightsheet Z.1 microscope system, which was operated by ZEN 2014 software (black edition). Embryos were first manually dechorionated and then mounted in 0.6% low-melting-point agarose (in E3) containing 240 µg ml^{-1} of tricane methane sulfonate (MS-222; Sigma-Aldrich), as previously described[56]. The sample chamber was filled with E3 medium supplemented with 0.2 mM PTU (Sigma-Aldrich) and 0.01% MS-222, and kept at 28.5 °C during imaging. The image stacks spanned 100.0 µm with 0.5 µm optical sectioning. Images were acquired at 5 min intervals for 3–4 h using the double-sided illumination mode by a Zeiss Plan-Apochromat ×20 water-dipping objective (Carl Zeiss Microscopy; numerical aperture, 1.0) with two Edge 5.5 scientific complementary metal–oxide–semiconductor cameras (PCO). Nuclei were manually tracked in four dimensions (4D) using TrackMate[57], an open-source Fiji plugin.

2D analysis of cells as well as nuclei sizes and shapes

Images of the retina (or brain) were acquired as described in the 'Imaging of retina and brain tissue structure' section. To reduce noise in the original images, we used ImageJ's 3D median filter of 1 pixel radius. We first detected the middle of each nucleus in three dimensions by finding their maximal cross-sectional area in the 3D stack. Then, we used the polygon selection tool in ImageJ to trace the outline of each cell and nucleus at the *z* plane corresponding to the 3D centre of each nucleus. Using the Fit Ellipse tool in ImageJ, we next extracted the following shape descriptors: area, major axis (primary axis of the best-fitting ellipse), minor axis (secondary axis of the best-fitting ellipse), aspect ratio (major axis/minor axis) and circularity, where circularity is used to compute the shape factor in the analysis.

Two-photon laser damage of nuclei

Samples were imaged on a confocal laser scanning microscope (Zeiss, LSM 980) using a ×40/1.1 C-Apochromat water-immersion objective (Zeiss). In each retina, we selected a nucleus to be analysed (nucleus #1, Supplementary Fig. 3a,b) and 3–6 (median, 4) of its direct neighbouring nuclei to ablate. Using a femtosecond laser (InSight STDS-AX, Spectra-Physics), we performed laser ablation in these neighbouring nuclei by applying a laser treatment on the square region of interest (0.4 µm × 0.4 µm) located at the centre of the nuclei to be damaged. We used the following parameters for ablation: pixel size, 0.41 µm; pixel dwell time, 1.02 µs; laser wavelength, 920 nm; laser output power, 450 mW; repetitions, 2 to 6 depending on the developmental stage and depth. We acquired one frame every 5 s, with two frames before ablation and 34 frames after ablation. We assessed the success of damage by the presence of a small autofluorescent point in the nucleus, physiological reaction of the tissue (deformation of the centre nucleus) and/or a posteriori confirmation of cell death (Supplementary Fig. 3d). In cases where the cell membrane was damaged, we observed intense ruffling, contraction of the damaged cell and quick arrival of immune cells. We discarded data showing such behaviour. In addition, for each experiment, we chose a nucleus located at least two nuclei away from the ablated nuclei as an unperturbed control (nucleus #2, Supplementary Fig. 3a,b). The shapes of both central (nucleus #1) and control (nucleus #2) nuclei were quantified as described in the '2D analysis of cells as well as nuclei sizes and shapes' section.

Nuclei labelling in fixed embryos

Embryos for immunostaining were manually dechorionated at 72 hpf, anaesthetized and fixed in 4% paraformaldehyde overnight at 4 °C and then rinsed in phosphate-buffered saline with 1% Tween 20 (PBST). Embryos were permeabilized by rinsing in pure water, immersing in prechilled acetone for 8 min at −20 °C, rinsing again in pure water and finally rinsing in PBST. Embryos were then incubated at room temperature for 1 h in a permeabilization buffer (PBS with 1% Tween 20, 3% Triton X-100 and 1% dimethyl sulfoxide). Finally, embryos were incubated in 1:1,000 DAPI diluted in a permeabilization buffer for 2 h at room temperature.

Generation and injection of ferrofluid droplets

Ferrofluid droplets were prepared as previously described[44]. Briefly, the ferrofluid consists of 80% (v/v) DFF2 (Ferrotec), 2% (w/w) Krytox-PEG 600 (008-FluoroSurfactant, RAN Biotechologies) and a custom-made fluorous soluble dye (either 25 µM FCy5 or 50 µM FCy7)[58] in Novec 7300 fluorocarbon oil (3M). The ferrofluid oil was calibrated before each experiment using a viscosity standard oil (N190000, Cannon) as previously described[6], allowing quantitative experiments with known magnetic stresses. We inserted the ferrofluid droplet into the INL region of the zebrafish retina (either *Tg*(*Bactin*:*HRAS-EGFP*); *Tg*(*h2az2a*:*h2az2a-mCherry*) or heat-shocked *Tg*(*hsp70*:*lmna-mKate2*)). To do this, we first mounted 68–70 hpf embryos on 3% agarose gel and treated with 0.02% (w/v) MS-222 and 0.2 mM PTU in E3 buffer to immobilize the larvae for injection and to continue the inhibition of further pigmentation. Then, a ferrofluid droplet (around 25 µm in diameter) was directly generated inside the INL of each zebrafish eye by direct microinjection using a custom-modified (40° bevelled and spiked) aluminosilicate glass needle (AF100-64-10, Sutter Instrument) with a picolitre injector (PLI-100A, Warner Instruments) under a Leica M205 FCA stereoscope. After microinjection, the injected larvae were washed with E3 buffer and then incubated at 28 °C in E3 buffer with 0.2 mM PTU to allow tissue recovery for at least 2 h before magnetic actuation.

Imaging of ferrofluid droplets during magnetic actuation

Imaging of ferrofluid droplets was done as previously described[6,44], using a confocal laser scanning microscope (LSM 980, Carl Zeiss). Briefly, for ferrofluid oil calibration, droplets in the viscosity reference oil were imaged under the confocal mode with a ×10 air objective (Plan-Apochromat, numerical aperture of 0.45, Carl Zeiss) at a frame rate of 1.7 s at 25 °C. For droplets in the INL of zebrafish retina, the droplet-injected zebrafish embryo (72 hpf) was anaesthetized by 0.02% (w/v) MS-222 and mounted in 1% (w/v) low-melting-point agarose in a 50 mm glass-bottom dish (P50G-1.5-14-F, MatTek) for imaging. The time-lapse imaging of magnetic actuation was performed using a ×40 water-immersion objective (LD C-Apochromat 1.1 W, Carl Zeiss) at a frame rate of 2 s. Retina of *Tg*(*Bactin*:*HRAS-EGFP*)^{vu119}; *Tg*(*h2az2a*:*h2az2a-mCherry*)^{tud7} transgenic zebrafish larvae with FCy5-labelled ferrofluid oil were imaged with 639 nm laser for excitation under the Airyscan mode. We used *Tg*(*hsp70*:*lmna-mKate2*) embryos, in which the overexpression of lamin A was previously induced on heat-shock in all nuclei to increase the lamin A levels. The heat-shocked *Tg*(*hsp70*:*lmna-mKate2*) transgenic embryos with an FCy7-labelled ferrofluid oil droplet previously inserted in the retina were imaged with 730 nm laser and a near-infrared detector with 760–900 nm emission filter (Carl Zeiss) using the confocal mode.

Magnetic actuation of ferrofluid microdroplets

The actuation of ferrofluid droplets was performed following the same protocol with identical magnetic actuation setup and custom-made LabVIEW (National Instruments) code for droplet analysis as previously described[44]. Briefly, a ferrofluid droplet embedded in the tissue was deformed by applying a uniform and constant magnetic field. On application of a uniform, constant magnetic field, ferrofluid droplets acquire an ellipsoidal shape. We monitored the time evolution of droplet deformation by quantifying the ellipsoidal shape, or the droplet strain $\varepsilon = 2(b/a - 1)/3$ defined previously[44], where a and b are

the minor and major axes of the ellipsoidal shape, respectively, with the major axis pointing in the direction of the applied magnetic field. To measure the linear mechanical response of the tissue, we applied magnetic fields leading to small strains (<0.2) for 2–10 min, as this timescale is longer than the relaxation timescales associated with subcellular processes[45], but short enough that no nuclear rearrangements are generated by actuation. We obtained the effective stiffness of the tissue from the time evolution of the strain on actuation, as previously described[44,45].

2D analysis of nuclei ordering

We manually identify the nuclei of retinal cells within the INL for ten retinae at 55 hpf and ten retinae at 120 hpf. For each sample, the nearest-neighbour relations were computed using Voronoi tessellation based on nuclei positions. The network configuration was constructed by connecting all the pairs of nearest neighbours. The bond length s and bond angle θ are defined in the same way as in the analysis of tissue structure in simulations (Fig. 2j,k). The deviation in tissue structure from the crystalline hexagonal structure was quantified by the standard deviation of the normalized bond length $\sigma_{s/\bar{s}}$ and bond angle $\sigma_{\theta/\bar{\theta}}$.

Statistics and reproducibility

In the experiments involving zebrafish embryos, no statistical methods were used to predetermine the sample sizes but our sample sizes are similar to those reported in previous publications. In nuclear damage experiments, we excluded data displaying clear damage to cell membranes. Analysis of all the data was done either by automated software or by investigators with no prior knowledge on allocation during experiments or outcome assessment to ensure blinding and avoid biases in the analysis. No randomization of the data was used.

Reporting summary

Further information on research design is available in the Nature Portfolio Reporting Summary linked to this article.

Data availability

The data supporting the findings of this study are included in the Article and its Supplementary Information files and are also available from the corresponding author upon request. Source data are provided with this paper.

Code availability

The simulation codes used in this Article are publicly available via GitHub at https://github.com/campaslab/active_foam_nucleus.

References

51. Nüsslein-Volhard, C. & Dahm, R. *Zebrafish* (Oxford Univ. Press, 2002).
52. Cooper, M. S. et al. Visualizing morphogenesis in transgenic zebrafish embryos using BODIPY TR methyl ester dye as a vital counterstain for GFP. *Dev. Dyn.* **232**, 359–368 (2005).
53. Xiong, F. et al. Specified neural progenitors sort to form sharp domains after noisy Shh signaling. *Cell* **153**, 550–561 (2013).
54. Knopf, F. et al. Bone regenerates via dedifferentiation of osteoblasts in the zebrafish fin. *Dev. Cell* **20**, 713–724 (2011).
55. Pauls, S., Geldmacher-Voss, B. & Campos-Ortega, J. A. A zebrafish histone variant H2A.F/Z and a transgenic H2A.F/Z:GFP fusion protein for in vivo studies of embryonic development. *Dev. Genes Evol.* **211**, 603–610 (2001).
56. Icha, J. et al. Using light sheet fluorescence microscopy to image zebrafish eye development. *J. Vis. Exp.* **110**, e53966 (2016).
57. Tinevez, J.-Y. et al. TrackMate: an open and extensible platform for single-particle tracking. *Methods* **115**, 80–90 (2017).
58. Lim, I. et al. Fluorous soluble cyanine dyes for visualizing perfluorocarbons in living systems. *J. Am. Chem. Soc.* **142**, 16072–16081 (2020).

Acknowledgements

We thank I. Lim, H. Lin and E. Sletten (University of California, Los Angeles) for sharing custom-made fluorinated dyes. We also thank C. Froeb for technical support, G. Stooke-Vaughan for her help and also for bringing the study of the retina to the Campas lab, M. Valet for her scientific advice and support and all the other Campas lab members for their help. We thank the Fish Facility of the Max Planck Institute of Molecular Cell Biology and Genetics (MPI-CBG) for their technical support, the MPI-CBG imaging facility (especially J. Peychl) for their advice and technical support on image acquisition and the MPI-CBG Transgenic core facility (J. Braumann and R. Naumann) for bevelling and spiking glass needles. This work was supported by the Eunice Kennedy Shriver National Institute of Child Health and Human Development of the National Institutes of Health (R01HD095797 to O.C.), and the Deutsche Forschungsgemeinschaft (DFG, German Research Foundation) under Germany's Excellence Strategy–EXC 2068–390729961–Cluster of Excellence Physics of Life of TU Dresden. We acknowledge support from the UCSB Center for Scientific Computing from the CNSI, MRL: NSF MRSEC (DMR-1720256) and NSF CNS-1725797.

Author contributions

S.K., R.A. and O.C. designed the research. S.K. performed all the simulations. R.A. performed all the structural experiments and measurements of nuclear movements. R.A., S.-T.Y. and P.P. performed the mechanical measurements. A.B. and R.A. performed the laser ablation experiments. S.K., R.A., P.P., A.B. and I.A.D. analysed the data. S.K., R.A. and O.C. wrote the paper, with input from S.-T.Y., P.P. and A.B. O.C. supervised the project.

Competing interests

The authors declare no competing interests.

Additional information

Extended data is available for this paper at https://doi.org/10.1038/s41563-024-01972-3.

Supplementary information The online version contains supplementary material available at https://doi.org/10.1038/s41563-024-01972-3.

Correspondence and requests for materials should be addressed to Otger Campàs.

Peer review information *Nature Materials* thanks Matthieu Piel and the other, anonymous, reviewer(s) for their contribution to the peer review of this work.

https://doi.org/10.1038/s41563-024-01972-3

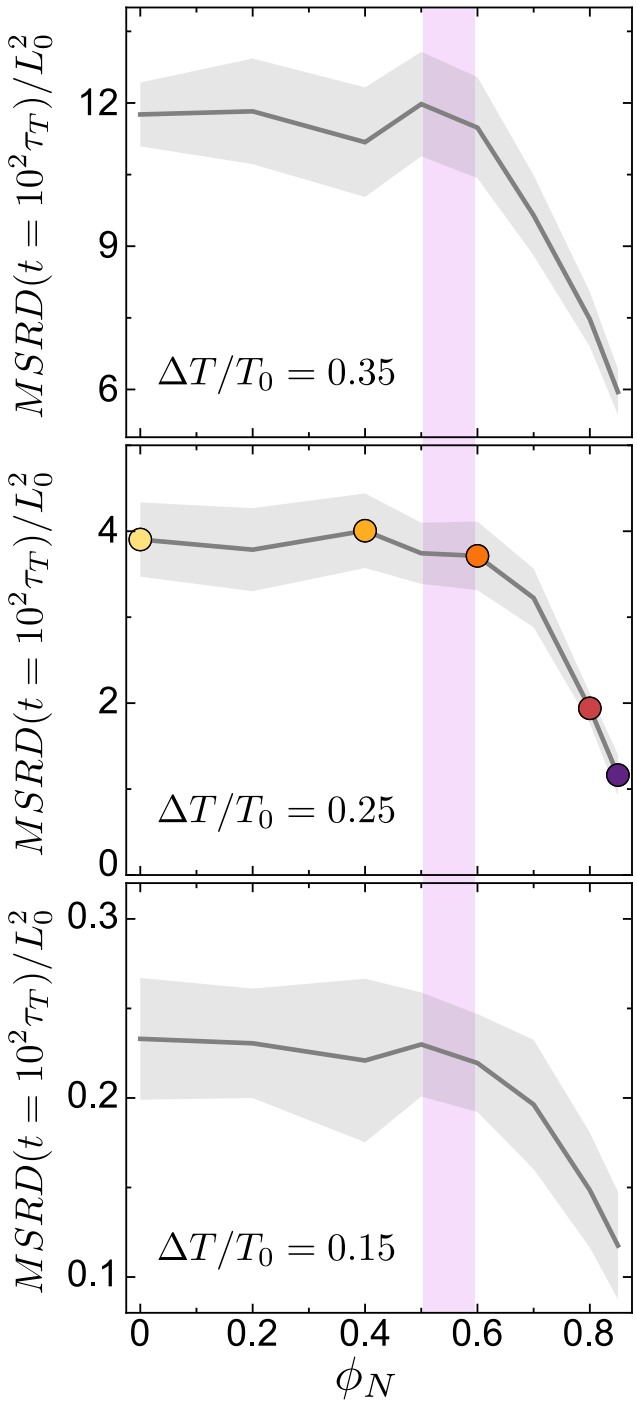

Extended Data Fig. 1 | Effects of the magnitude of tension fluctuations on the nuclear jamming transition. Dependence of long timescale MSRD values in terms of nuclear volume fraction for different magnitudes of tension fluctuations $\Delta T/T_0$, showing that the dynamic slowdown in cell movements starts to occur at the same nuclear volume fraction (violet band) regardless of tension fluctuation strength. Error bands indicate standard deviation over N = 10 simulations.

https://doi.org/10.1038/s41563-024-01972-3

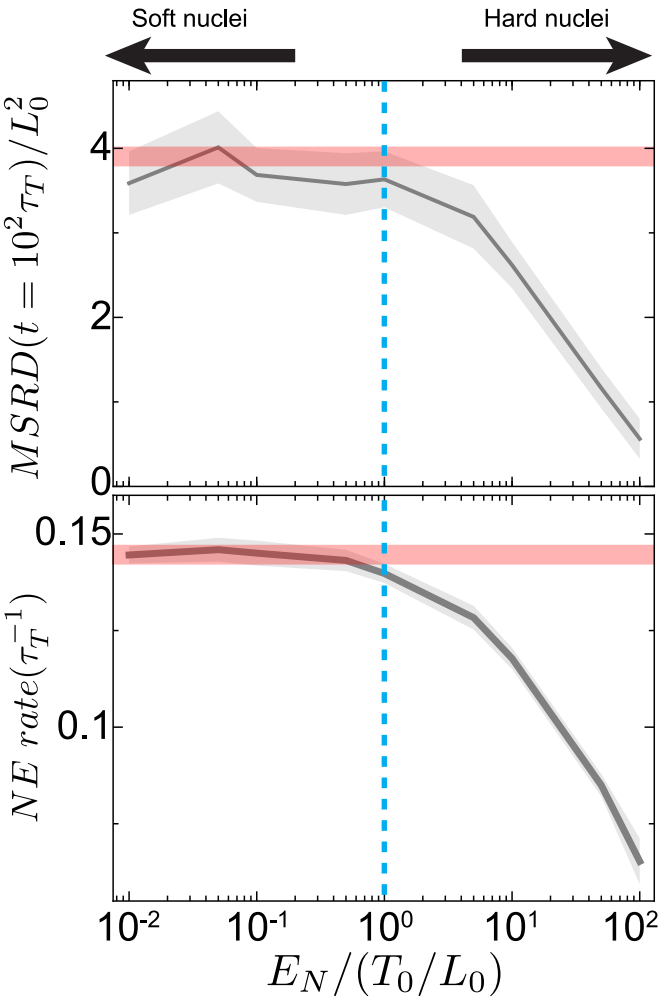

Extended Data Fig. 2 | Effects of nuclear stiffness on the nuclear jamming transition. Dependence of the long timescale MSRD values (top) and neighbor exchange rate (bottom) for large nuclear volume fraction ($\phi_N = 0.85$) on the ratio of nuclear stiffness E_N and the characteristic stress scale of cell deformations T_0/L_0. Large (small) values of $E_N/(T_0/L_0)$ indicate hard (soft) nuclei compared to the cell. Red lines are the values of long time MSRD and neighbor exchange rate for zero nuclear volume fraction ($\phi_N = 0$), and the vertical cyan dashed line indicates the point at which nuclear stiffness and the stress scale of cell deformations are equal, namely $E_N = T_0/L_0$. Error bands indicate standard deviation over N = 10 simulations.

https://doi.org/10.1038/s41563-024-01972-3

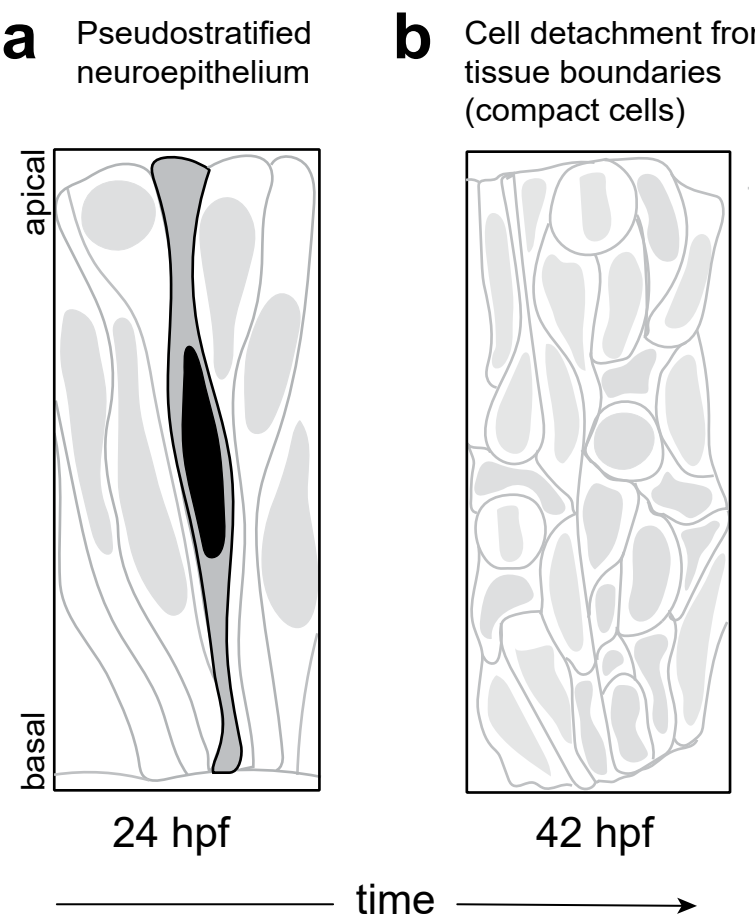

Extended Data Fig. 3 | Schematic representation of the zebrafish retina before and after cell detachment from apical and basal tissue boundaries. **a**, The zebrafish is a single-layered neuroepithelium with elongated cells connected to both the apical and basal tissue surfaces at 24 hpf. **b**, At approximately 40–42 hpf, majority of retinal cells detach from the tissue (apical and basal) boundaries and form a tissue with compact cells. This single-layered tissue eventually evolves into the different layers described in the main text (Fig. 3).

https://doi.org/10.1038/s41563-024-01972-3

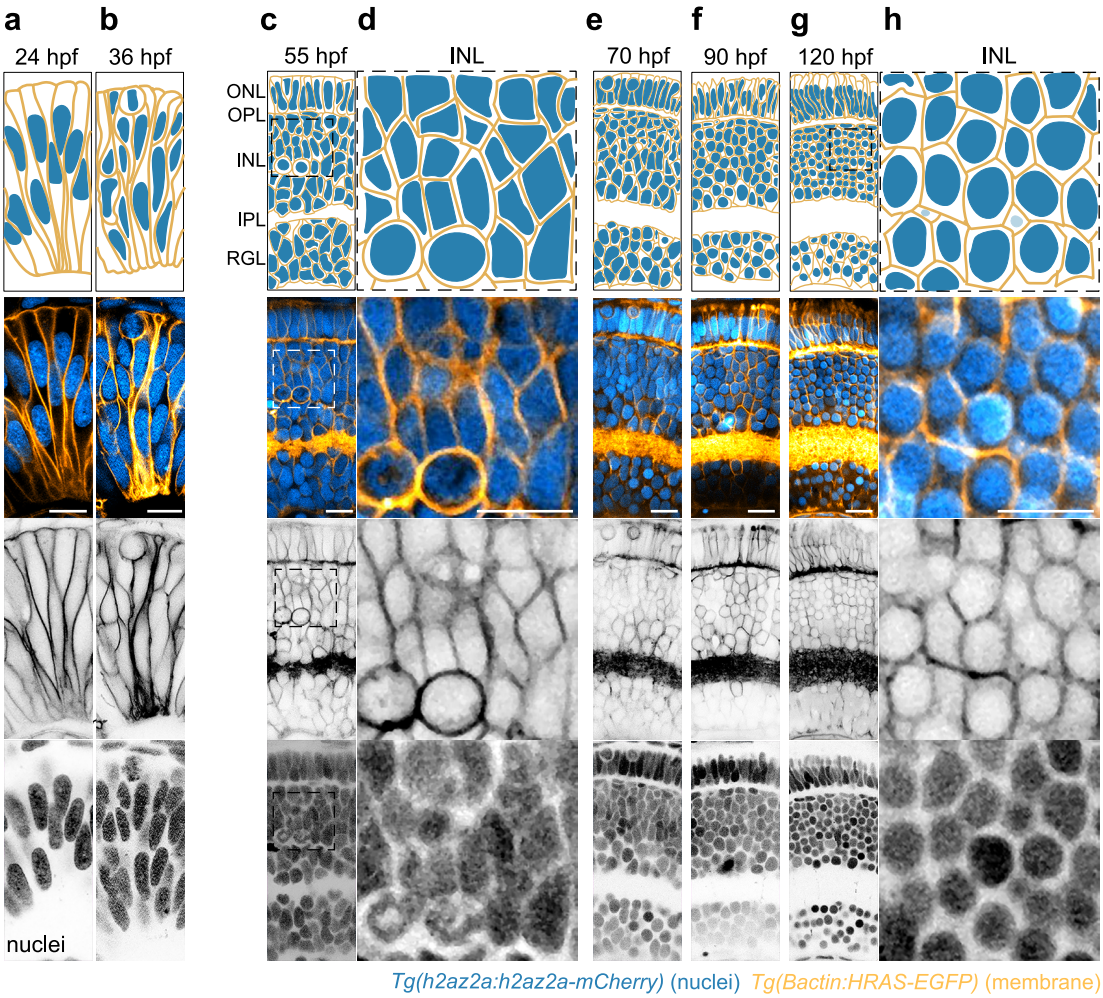

Extended Data Fig. 4 | Tissue architecture during retina development: evolution of cell and nuclear shapes and sizes. a-h, Top: schematic representation of cellular and nuclear architecture during different retinal stages (a, 24; b, 36; c, 55; e, 72; f, 92; g, 120 hpf). Bottom: Representative confocal sections of zebrafish retinae expressing the membrane marker (*Tg(Bactin:HRAS-EGFP)*; orange) and nuclei marker *Tg(h2az2a:h2az2a-mCherry)*; cyan). Scale bars, 20 µm. **d, h**, Higher magnification inset of the outlined region in (c), and (g) respectively. Scale bars, 10 µm.

https://doi.org/10.1038/s41563-024-01972-3

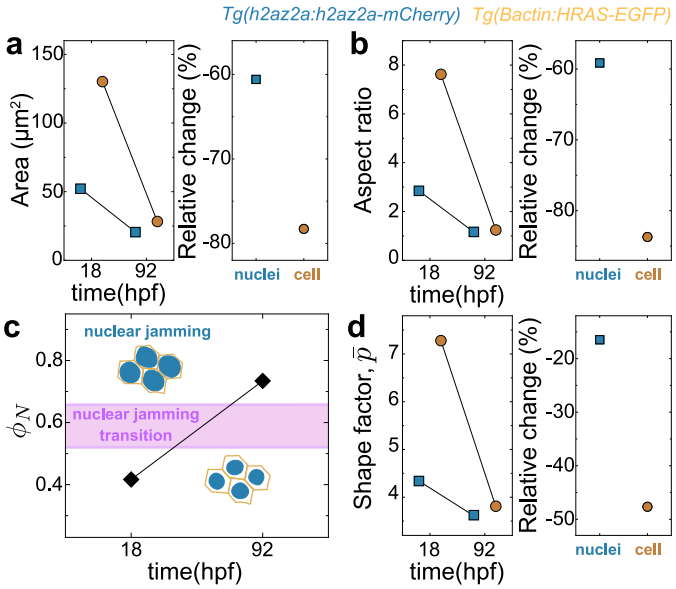

Extended Data Fig. 5 | Different brain regions show nuclear jamming. Areas (**a**) and aspect ratios (**b**) of cells (orange) and nuclei (blue) in the MB (18 hpf) and OT (92 hpf). Their relative change between 18 to 92 hpf is plotted on the right panels. **c**, Nuclear volume fraction in the MB (18 hpf) and in the OT (92 hpf). Horizontal violet band shows the nuclear jamming volume fraction predicted theoretically (Fig. 2). **d**, Shape factor of cells (orange) and nuclei (blue) in the MB (18 hpf) and OT (92 hpf). Their relative change between 18 to 92 hpf is plotted on the right panels. MB (N = 6, n = 312), OT (N = 6, n = 419).

nature research

Corresponding author(s): Otger Campas

Last updated by author(s): Jun 17, 2024

Reporting Summary

Nature Research wishes to improve the reproducibility of the work that we publish. This form provides structure for consistency and transparency in reporting. For further information on Nature Research policies, see our Editorial Policies and the Editorial Policy Checklist.

Statistics

For all statistical analyses, confirm that the following items are present in the figure legend, table legend, main text, or Methods section.

n/a	Confirmed	
☐	☒	The exact sample size (*n*) for each experimental group/condition, given as a discrete number and unit of measurement
☐	☒	A statement on whether measurements were taken from distinct samples or whether the same sample was measured repeatedly
☒	☐	The statistical test(s) used AND whether they are one- or two-sided *Only common tests should be described solely by name; describe more complex techniques in the Methods section.*
☒	☐	A description of all covariates tested
☒	☐	A description of any assumptions or corrections, such as tests of normality and adjustment for multiple comparisons
☐	☒	A full description of the statistical parameters including central tendency (e.g. means) or other basic estimates (e.g. regression coefficient) AND variation (e.g. standard deviation) or associated estimates of uncertainty (e.g. confidence intervals)
☒	☐	For null hypothesis testing, the test statistic (e.g. *F*, *t*, *r*) with confidence intervals, effect sizes, degrees of freedom and *P* value noted *Give P values as exact values whenever suitable.*
☒	☐	For Bayesian analysis, information on the choice of priors and Markov chain Monte Carlo settings
☒	☐	For hierarchical and complex designs, identification of the appropriate level for tests and full reporting of outcomes
☒	☐	Estimates of effect sizes (e.g. Cohen's *d*, Pearson's *r*), indicating how they were calculated

Our web collection on statistics for biologists contains articles on many of the points above.

Software and code

Policy information about availability of computer code

Data collection	A Multiphoton Laser Scanning Confocal Microscope (2-photon inverted microscope; Leica, SP8) and a Laser Scanning Confocal Microscope (Zeiss, LSM780; Zen Black) were used for 3D scans of brain and retina samples. A laser scanning confocal microscope (Zeiss, LSM980; Zen Blue) was used for time-lapse imaging of nuclei movements (24 hpf, 92 hpf), laser ablation experiments, imaging of ferrofluid droplets, time-lapse imaging of magnetic actuation. The Zeiss Light Sheet Z.1 microscope system operated by ZEN 2014 software (black edition) was used for the time-lapse imaging of nuclear movements at 55 hpf. A custom-written software (LabVIEW, National Instruments) was used to synchronize the movement of the magnet array with image acquisition (using either a camera or the confocal microscope), and to control both the translation and rotation stages during magnetic actuation experiments.
Data analysis	Commercial software used to analyze data: Matlab 9.11 and 9.14 (MathWorks), Origin 2023. ImageJ was also used to analyze data. The aspect ratio of the droplet ellipsoidal deformation was determined using a previously-developed software in LabVIEW (National Instruments), publicly available from ref. 44.

For manuscripts utilizing custom algorithms or software that are central to the research but not yet described in published literature, software must be made available to editors and reviewers. We strongly encourage code deposition in a community repository (e.g. GitHub). See the Nature Research guidelines for submitting code & software for further information.

Data

Policy information about availability of data

All manuscripts must include a data availability statement. This statement should provide the following information, where applicable:

- Accession codes, unique identifiers, or web links for publicly available datasets
- A list of figures that have associated raw data
- A description of any restrictions on data availability

Source data are provided with this paper.

Field-specific reporting

Please select the one below that is the best fit for your research. If you are not sure, read the appropriate sections before making your selection.

☒ Life sciences ☐ Behavioural & social sciences ☐ Ecological, evolutionary & environmental sciences

For a reference copy of the document with all sections, see nature.com/documents/nr-reporting-summary-flat.pdf

Life sciences study design

All studies must disclose on these points even when the disclosure is negative.

Sample size	In experiments involving zebrafish embryos, no statistical methods were used to pre-determine sample sizes but our sample sizes are similar to those reported in previous publications (Refs. 44, 45).
Data exclusions	In nuclear damage experiments, we excluded data displaying clear damage to cell membranes.
Replication	Independent experiments were performed and statistical analysis done independently of these data sets. The results obtained were the same within error bars in different, independent data sets.
Randomization	No randomization of the data was used.
Blinding	Analysis of all the data was done either by automated software or by investigations with no prior knowledge on allocation during experiments or outcome assessment to ensure blinding and avoid biases in the analysis.

Reporting for specific materials, systems and methods

We require information from authors about some types of materials, experimental systems and methods used in many studies. Here, indicate whether each material, system or method listed is relevant to your study. If you are not sure if a list item applies to your research, read the appropriate section before selecting a response.

Materials & experimental systems

n/a	Involved in the study
☒	☐ Antibodies
☒	☐ Eukaryotic cell lines
☒	☐ Palaeontology and archaeology
☐	☒ Animals and other organisms
☒	☐ Human research participants
☒	☐ Clinical data
☒	☐ Dual use research of concern

Methods

n/a	Involved in the study
☒	☐ ChIP-seq
☒	☐ Flow cytometry
☒	☐ MRI-based neuroimaging

Animals and other organisms

Policy information about studies involving animals; ARRIVE guidelines recommended for reporting animal research

Laboratory animals	Zebrafish (Danio rerio) were used in this study. Since only embryos were studied, sex-specific experiments were not necessary, as zebrafish embryos at the studies stage have not yet undergone sex determination.
Wild animals	None.
Field-collected samples	None.
Ethics oversight	Experiments were performed following all ethical regulations and according to protocols approved by the European Union (EU) directive 2010/63/EU as well as the German Animal Welfare act.

Note that full information on the approval of the study protocol must also be provided in the manuscript.